J. Fluid Mech. (2010), *vol.* 661, *pp.* 206–228. © Cambridge University Press 2010
doi:10.1017/S0022112010002910

On the instability of a free viscous rim

ILIA V. ROISMAN†

Institute of Fluid Mechanics and Aerodynamics, Center of Smart Interfaces, Technische Universität Darmstadt, Petersenstr. 30, 64287, Darmstadt, Germany

(Received 10 October 2007; revised 18 May 2010; accepted 21 May 2010; first published online 27 July 2010)

This paper is devoted to the theoretical description of the dynamics of a rim formed by capillary forces at the edge of a free, thin liquid sheet. The rim dynamics are described using a quasi-one-dimensional approach accounting for the inertia of the liquid in the rim and for the liquid flow entering the rim from the sheet, surface tension and viscous stresses. The governing equations are derived from the mass, momentum and moment-of-momentum-balance equations of the rim. The theory provides a basis from which to analyse the linear stability of a straight line rim bounding a planar liquid sheet. The combined effect of the axisymmetric disturbances of the radius of the rim cross-section as well as of the transverse disturbances of the rim centreline is considered. The effect of the viscosity, relative film thickness and rim deceleration are investigated. The predicted wavelength of the most unstable mode is always very similar to the Rayleigh wavelength of the instability of an infinite cylindrical jet. This prediction is confirmed by various experimental data found in the literature. The maximum rate of growth of rim disturbances depends on all the parameters of the problem; however, the most pronounced effect can be attributed to the rim deceleration. This conclusion is confirmed by nonlinear simulations of rim deformation.

Key words: breakup/coalescence, capillary flows, instability

1. Introduction

Flow of a free, thin liquid sheet is relevant to many industrial applications such as polymer or foam processing, cooling, coating, washing, as well as in various hydrodynamic rheological experiments. The dynamics of free liquid sheets is determined by the inertia, viscous stresses and surface tension. The description of the liquid flow in the film can be significantly simplified by accounting for the smallness of the film thickness in comparison with the typical lengths in the other two directions. Such a simplifying approach has been used in the past to predict the shape of a steady flow in a liquid bell (Boussinesq 1869*a*, *b*; Taylor 1959*a*), the instability of free planar sheets (Taylor 1959*b*, *c*) and recently of an axisymmetric liquid sheet (Clanet 2001). Entov (1982) developed a quasi-two-dimensional theory describing the dynamics of thin films of viscous Newtonian liquids and polymeric solutions.

At the free edges of a free, stationary, uniform liquid film, the surface tension can be balanced only by the inertia of the liquid. Capillary forces are responsible for the emergence of a free rim propagating towards the liquid film with a finite velocity

† Email address for correspondence: roisman@sla.tu-darmstadt.de

(Taylor 1959*b*; Culick 1960):

$$V = \left[\frac{2\sigma}{\rho h_S}\right]^{1/2}, \tag{1.1}$$

where ρ and σ are the liquid density and surface tension, respectively, h_S is the thickness of the free sheet and V is the relative steady rim velocity in the direction normal to the rim centreline. Expression (1.1) is valid for low-viscosity liquids (Savva & Bush 2009).

The theoretical model of Entov *et al.* (1986) for the stationary rim bounding a planar sheet accounts for the flow and internal stresses in the rim and in the free film. Clanet & Villermaux (2002) have recently applied the rim dynamic equations to describe the stationary shape of the rim that arises when a radially expanding liquid sheet collides with an obstacle.

Many physical phenomena can be explained by the propagation of the rim, which include the spreading and receding of a drop impacting onto a dry partially wettable substrate (Roisman, Rioboo & Tropea 2002; Rozhkov, Prunet-Foch & Vignes-Adler 2002; Bartolo, Josserand & Bonn 2005), dewetting of a dry substrate (Brochard-Wyart, Di Meglio & Quéré 1987; Brochard-Wyart & De Gennes 1997), aerodynamic drop deformation by a shock wave (Hsiang & Faeth 1992, 1995), drop binary collisions (Ashgriz & Poo 1990; Brenn, Valkovska & Danov 2001; Roisman 2004) and the interaction of two jets (Bush & Hasha 2004). In some cases the rim becomes unstable, which leads to the emergence of finger-like jets that subsequently break up into drops. The jets appear usually in the plane of the film. One of the most important phenomena related to rim instability is the atomization of a liquid by a fan spray sheet (Clark & Dombrowski 1972) or pressure swirl atomizers, and secondary atomization by spray/wall or drop/substrate interaction (Yarin & Weiss 1995).

Comprehensive reviews on the topics of liquid fragmentation, breakup and atomization can be found in Lin & Reitz (1998), Villermaux (2007), Gorokhovski & Herrmann (2008), Eggers & Villermaux (2008) and Eggers (1997). Rim instability is often related to the capillary instability of a free infinite cylindrical jet. Rayleigh (1879) obtained the dispersion relation for an inviscid problem in the form

$$\omega = \sqrt{\frac{\sigma}{\rho a_0}}\left[\frac{\xi \mathrm{I}_n'(\xi)}{\mathrm{I}_n(\xi)}(1-n^2-\xi^2)\right]^{1/2}, \tag{1.2}$$

where ω is the growth rate of the disturbances, $\xi = 2\pi a_0/\ell$ is the dimensionless wavenumber (ℓ being the wavelength) and $\mathrm{I}_n(\xi)$ is the modified Bessel function of order n. The maximum growth rate of the axisymmetric disturbances ($n=0$) is $\omega_* = 0.343\sqrt{\sigma/(\rho a_0)}$ at $\xi = \xi_* = 0.697$.

Viscous effects are accounted for in the long-wave approximation in the work of Weber (1931) for the axisymmetric disturbances of a jet. The dispersion relation and the expression obtained for the wavenumber of the most unstable mode are

$$\omega = \sqrt{\frac{\sigma}{\rho a_0}}\left[\sqrt{2+(9Oh^2-2)\,\xi^2}-3Oh\xi\right]\frac{\xi}{2}, \tag{1.3a}$$

$$\xi_* = [2+3\sqrt{2}Oh]^{-1/2}, \tag{1.3b}$$

$$\omega_* = \sqrt{\frac{\sigma}{\rho a_0}}\,\frac{\sqrt{2+6\sqrt{2}Oh+9Oh^2}-3Oh}{4+6\sqrt{2}Oh}, \tag{1.3c}$$

where $Oh = \mu/\sqrt{\rho\sigma a_0}$ is the Ohnesorge number.

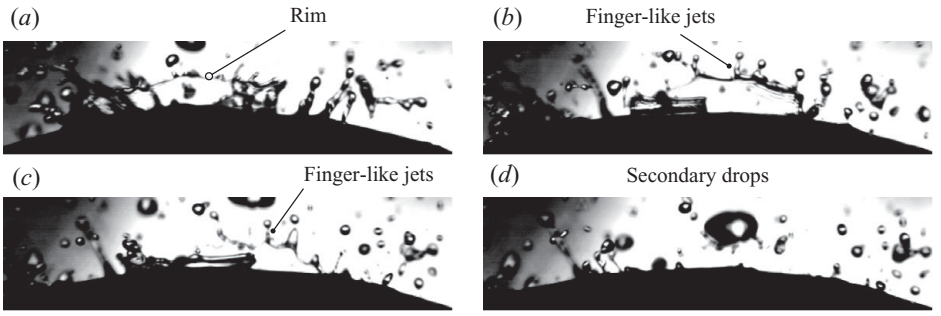

FIGURE 1. Unstable liquid sheets, jets and secondary drops generated by spray impact.

In the inviscid limit, $Oh = 0$, the most unstable mode predicted by the long-wave approximation of Weber is $\omega_* = 0.354\sqrt{\sigma/(\rho a_0)}$ at $\xi = \xi_* = 0.707$, which is close to the exact solution of Rayleigh. From the solution of Weber (1931) the eigenvector of the system can be found easily. This solution yields the ratio u_0/α_0 of the amplitudes of the longitudinal velocity and the disturbance of the rim radius. This ratio can be expressed in the form

$$u_0/\alpha_0 = \left[1 + \frac{3Oh}{\sqrt{2}}\right]^{-1/2}. \tag{1.4}$$

The jet stability and the wavelength of the most unstable mode can be significantly influenced by longitudinal stretching (Frankel & Weihs 1985; Khakhar & Ottino 1987) or by hydrodynamic forces applied from the surrounding fluid (Tomotika 1935; Entov & Yarin 1984; Brenner, Lister & Stone 1996).

Rim dynamics and stability are influenced by the flow entering the rim from the free sheet and by the capillary forces. These two factors often lead to rim stabilization. Fullana & Zaleski (1999) performed numerical simulations of rim propagation and deformation using the volume-of-fluid method. In their simulations rim-radius disturbances do not grow significantly and also do not lead to rim breakup. In the recent numerical study of Bagué, Zaleski & Josserand (2007) an initially stationary rim starts to propagate towards a uniform stationary liquid film. It is accelerated by the surface tension and then it deforms. The deformation of the rim centreline in some cases leads to the appearance of cusps (regions at which the radius of curvature of the rim centreline vanishes), ejection of a finger-like jet and drop formation.

The flow in finger-like jets appearing as the result of rim instability is usually almost parallel to the plane of the free liquid sheet and is directed nearly normal to the rim centreline. Consider, for example, the shape and the breakup of the unstable rim bounding a liquid sheet emerging as a result of spray impacting onto a rigid wall, as shown in figure 1. A stability analysis of a straight, infinite cylindrical jet cannot describe the emergence of the finger-like jets and the rim breakup since the considered disturbances to the rim are symmetrical relative to the rim centreline. Therefore, Rayleigh–Plateau instability alone cannot be responsible for splash despite the fact that this analysis well predicts the experimental data for the rim-breakup length (Deegan, Brunet & Eggers 2008). We repeat that one of the conclusions of the Rayleigh–Plateau analysis is that the fastest-growing disturbance of an infinite cylinder is axisymmetric. However, the observed rim deformation is not always axisymmetric. For the same reason the Richtmyer–Meshkov instability too (Krechetnikov & Homsy 2009), in our opinion, cannot be considered as the main reason for splash.

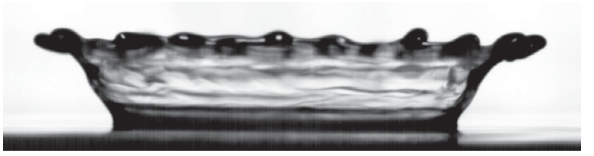

FIGURE 2. Splash produced by a single-drop impact onto a smooth, rigid, wetted substrate.

The linear stability of the inviscid rim has been analysed in Roisman, Horvat & Tropea (2006), accounting for the factors associated with the film flow. Linearized equations of motion for a nearly straight rim are derived from the mass, momentum and angular-momentum-balance equations. Both the axisymmetric disturbances of the radius of the rim cross-section and the transverse disturbances of the rim centreline are considered. The growth rate of the disturbances of rim increases significantly with the rim acceleration towards the film and decreases with the relative film thickness. The wavelength of the most unstable mode is very similar to the wavelengths obtained by Rayleigh (1879) and Weber (1931) for a wide range of the parameters.

In a recent study of spray impact (Roisman *et al.* 2007), the effect of film stretching was investigated. It was shown that strong film stretching can lead to the appearance of long stable portions of the rim. Corresponding experimental evidence of their theoretical predictions are provided in Roisman *et al.* (2007).

It should be noted that the reason for rim instability and the mechanisms of splash are still rather disputed subjects. One important topic which is not considered in our previous theory on rim transverse bending (Roisman *et al.* 2006, 2007) is the shape of the rim. These studies have concentrated solely on the shape of the centreline whose deformation could lead to cusp formation, as suggested by Yarin & Weiss (1995). In fact, at the instant of the emergence of a finger-like jet the disturbance of the rim centreline is frequently not clearly visible. One such example is shown in figure 2. The jets originate from the bumps distributed along the rim and growing in the direction of motion of the rim centreline. One possible explanation for the bumps' formation is with respect to the instability of the internal flow inside the rim, leading to the deformation of the rim cross-section. In this paper, we show that this phenomenon can be explained in the framework of the long-wave approximation of a quasi-two-dimensional theory on rim dynamics.

The main topic of this study is the development of a theoretical model for the evolution of a rim bounding a free viscous sheet. The theory combines a quasi-one-dimensional approach to the dynamics of a free cylindrical jet and a quasi-two-dimensional approach to the dynamics of a free, thin liquid sheet (Yarin 1993). In § 2 the governing equations for the propagation of the rim centreline, growth of the size of the rim cross-section and the internal liquid flow in the rim are obtained from the mass, momentum and moment-of-momentum-balance equations, accounting for capillary forces, internal viscous stresses in the rim and in the film, as well as the inertia of the flow in the rim and of the flow entering the rim from the liquid sheet. In § 3 the theory is applied to the linear stability analysis of a nearly straight rim. The results of the stability analysis are discussed in § 4. In particular, the effect of viscosity on the maximum growth rate of the disturbances and on the corresponding wavelength is investigated. The predicted shape of the perturbed rim is similar to the form observed in experiments.

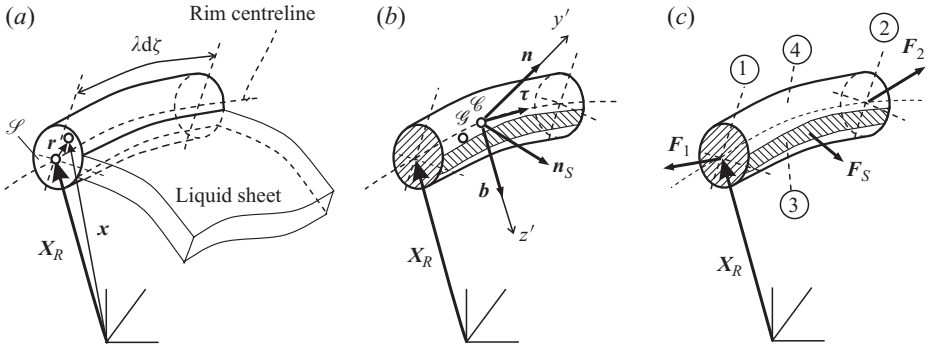

FIGURE 3. Element $\mathrm{d}\zeta$ of a free rim. (a) Geometry of the rim, (b) definition of the coordinate system and (c) the surface forces applied to the rim element.

2. Dynamics of a rim

2.1. *Definition of the coordinate system and geometry of the rim centreline*

Consider a median surface of a free sheet in parametric form as $\boldsymbol{x} = \boldsymbol{X}_S(\boldsymbol{\xi}, t)$ and the average velocity in the sheet as $\boldsymbol{u}_S(\boldsymbol{\xi}, t)$, where $\boldsymbol{\xi}$ is a vector of two parameters and t is time. Also define a unit normal vector $\boldsymbol{N}_S$ to the surface $\boldsymbol{x} = \boldsymbol{X}_S(\boldsymbol{\xi}, t)$.

Also consider a free rim bounding a free sheet (figure 3). Here the centreline of the rim is defined in parametric form as $\boldsymbol{x} = \boldsymbol{X}_R(\zeta, t)$, where ζ is a parameter associated with a material point moving with the rim. The area of the rim cross-section $\mathscr{S}$ is denoted by $A(\zeta, t)$ and the thickness of the liquid film at the rim location is $h_{SR}(\zeta, t)$. Consider then a coordinate system $\{s', y', z'\}$ with its origin at the rim centreline and the corresponding unit vectors $\{\boldsymbol{\tau}, \boldsymbol{n}, \boldsymbol{b}\}$, where $\boldsymbol{\tau}$ is the unit tangent vector to the curve $\boldsymbol{x} = \boldsymbol{X}_R$, $\boldsymbol{n}$ is the unit principal normal and $\boldsymbol{b}$ is the unit binormal vector, as shown in figure 3(b). Denote a unit vector $\boldsymbol{n}_S = \boldsymbol{\tau} \times \boldsymbol{N}_S$ normal to the rim centreline and parallel to the sheet surface. Any radius vector $\boldsymbol{x}$ can be represented in the form $\boldsymbol{x} = \boldsymbol{X}_R + \boldsymbol{r}$, where $\boldsymbol{r}$ is the radius vector in the moving system $\{\boldsymbol{\tau}, \boldsymbol{n}, \boldsymbol{b}\}$.

The length of the element $\mathrm{d}\zeta$ of the rim at the centreline is $\lambda \mathrm{d}\zeta$, where the rim stretching parameter λ is defined through $\lambda = |\boldsymbol{X}_{R,\zeta}|$. The unit base vectors can now be defined in the form

$$\boldsymbol{\tau} = \lambda^{-1} \boldsymbol{X}_{R,\zeta}, \qquad \boldsymbol{n} = \boldsymbol{\tau}_{,\zeta} \, |\boldsymbol{\tau}_{,\zeta}|^{-1}, \qquad \boldsymbol{b} = \boldsymbol{\tau} \times \boldsymbol{n}. \tag{2.1}$$

The relationship between the base vectors and the local curvature, κ, and torsion, τ, of the centreline can be obtained from the Serret–Frenet formulae:

$$\boldsymbol{\tau}_{,\zeta} = \lambda \kappa \boldsymbol{n}, \qquad \boldsymbol{n}_{,\zeta} = \lambda(-\kappa \boldsymbol{\tau} + \tau \boldsymbol{b}), \qquad \boldsymbol{b}_{,\zeta} = -\lambda \tau \boldsymbol{n}. \tag{2.2}$$

Denoting the centre of mass of the rim volume element $\mathscr{G}$ and the centre of mass of the rim cross-section by $\mathscr{C}$, the position of the point $\mathscr{G}$ is determined as $\boldsymbol{r} = \boldsymbol{r}_G$, whereas the position of the centre of mass $\mathscr{C}$ of the cross-section $\mathscr{S}$ is $\boldsymbol{r} = 0$ by definition. For an element of the rim cross-section denoted by $\mathrm{d}\mathscr{S}$, an element of the rim volume can be defined as $\lambda(1 - \kappa y') \, \mathrm{d}\mathscr{S} \, \mathrm{d}\zeta$, such that the positions of the points

$\mathscr{C}$ and $\mathscr{G}$ are defined through

$$\boldsymbol{r}_C = \frac{\int_{\mathscr{S}} (y'\boldsymbol{n} + z'\boldsymbol{b})\,\mathrm{d}\mathscr{S}}{A} \equiv 0, \tag{2.3a}$$

$$\boldsymbol{r}_G = \frac{\int_{\mathscr{S}} (y'\boldsymbol{n} + z'\boldsymbol{b})\,\lambda(1-\kappa y')\,\mathrm{d}\mathscr{S}\,\mathrm{d}\zeta}{\int_{\mathscr{S}} \lambda(1-\kappa y')\,\mathrm{d}\mathscr{S}\,\mathrm{d}\zeta} = -\frac{\kappa}{A}(I_b\boldsymbol{n} - I_{bn}\boldsymbol{b}), \tag{2.3b}$$

where

$$I_b = \int_{\mathscr{S}} y'^2\,\mathrm{d}\mathscr{S}, \quad I_{bn} = \int_{\mathscr{S}} y'z'\,\mathrm{d}\mathscr{S}, \quad A = \int_{\mathscr{S}} \mathrm{d}\mathscr{S}, \tag{2.4}$$

with I_b and I_{bn} being the moments of inertia of the rim cross-section; I_{bn} vanishes for a symmetrical rim cross-section.

The relative velocity $\boldsymbol{w}(\boldsymbol{r}, \zeta, t)$ in the cross-section $\mathscr{S}$ is associated with rim stretching, deformation and circulation induced by the flow entering from the liquid film. Therefore, the absolute velocity $\boldsymbol{v}$ in $\mathscr{S}$ can be expressed as

$$\boldsymbol{v} = \boldsymbol{V} + \boldsymbol{\Omega} \times \boldsymbol{r} + \boldsymbol{w}, \tag{2.5}$$

where

$$\boldsymbol{V}(\zeta, t) = \boldsymbol{X}_{R,t}, \qquad \boldsymbol{\Omega} = (\boldsymbol{n}_{,t} \cdot \boldsymbol{b})\boldsymbol{\tau} - (\boldsymbol{\tau}_{,t} \cdot \boldsymbol{b})\boldsymbol{n} + (\boldsymbol{\tau}_{,t} \cdot \boldsymbol{n})\boldsymbol{b} \tag{2.6}$$

are the velocity of the centreline and the angular velocity of the cross-section $\mathscr{S}$.

The components of the angular velocity are obtained from (2.1), (2.6) and (2.2) as

$$\Omega_n = -\lambda^{-1} V_{b,\zeta} - \tau V_n, \quad \Omega_b = \lambda^{-1} V_{n,\zeta} + \kappa V_\tau - \tau V_b, \tag{2.7}$$

$$\Omega_\tau = [\lambda^{-1} V_{b,\zeta}]_{,\zeta} + \lambda^{-1}[\lambda\tau V_n]_{,\zeta} + \lambda\kappa\tau V_\tau - \lambda\tau^2 V_b. \tag{2.8}$$

The values of Ω_n and Ω_b are the same as obtained by Entov & Yarin (1984) for a free liquid jet.

2.2. *Rim-balance equations*

In order to formulate the rim-balance equations the surface determining the element of the rim is subdivided into four regions (figure 3*c*). Regions 1 and 2 are the cross-sections of the rim, region 3 is the interface between the rim and the sheet and region 4 is the free surface of the rim. The unit vectors $\boldsymbol{\tau}_1$ and $\boldsymbol{\tau}_2$ are normal to the cross-sections 1 and 2, whereas the unit vector $\boldsymbol{n}_S$ is normal to area 3.

The mass balance is written in the Lagrangian form as follows:

$$(\lambda A)_{,t} = h_{SR}\lambda(\boldsymbol{V} - \boldsymbol{u}_{SR}) \cdot \boldsymbol{n}_S(1 - \kappa y'_S), \tag{2.9}$$

where $\boldsymbol{u}_{SR}$ is the average velocity of the liquid in the liquid film at the position of the rim and y'_S is the coordinate of the mouth of the sheet entering the rim. The forces $\boldsymbol{F}_1$ and $\boldsymbol{F}_2$ (corresponding to the stretching of the rim) are applied to surfaces 1 and 2, and the force $\boldsymbol{F}_S$ is applied to surface 3 from the film. The force $\boldsymbol{F}_S$ consists of the surface tension (of two free surfaces of the liquid film) and of the force associated with the viscous stresses in the liquid film:

$$\boldsymbol{F}_S = (2\sigma\boldsymbol{n}_S + h_{SR}\boldsymbol{\sigma}_S \cdot \boldsymbol{n}_S)\lambda\,\mathrm{d}\zeta(1 - \kappa y'_S), \tag{2.10}$$

where $\boldsymbol{\sigma}_S$ is the average stress tensor in the liquid film. The total force $\boldsymbol{F}$ applied to the cross-section of the rim can be subdivided into the longitudinal, $P\boldsymbol{\tau}$, and shear, $\boldsymbol{Q}$, components.

The momentum balance of the element of the rim can be easily expressed in the system moving with the centre of mass $\mathscr{G}$:

$$\rho A(\boldsymbol{V}_{,t} + \boldsymbol{r}_{G,tt}) = (2\sigma \boldsymbol{n}_S + h_{SR}\boldsymbol{\sigma}_S \cdot \boldsymbol{n}_S)(1 - \kappa y'_S) - \rho h_{SR}[(\boldsymbol{u}_{SR} - \boldsymbol{V}) \cdot \boldsymbol{n}_S](\boldsymbol{u}_{SR} - \boldsymbol{V})(1 - \kappa y'_S) + \lambda^{-1}\boldsymbol{F}_{,\xi}. \quad (2.11)$$

The angular momentum of the element of the rim is defined as

$$\mathrm{d}\boldsymbol{L} = \boldsymbol{l}\,\lambda\,\mathrm{d}\zeta, \quad \text{with} \quad \boldsymbol{l} = \int_{\mathscr{S}} (1 - \kappa y')\,\boldsymbol{x} \times \rho\,\boldsymbol{v}\,\mathrm{d}\mathscr{S}, \quad (2.12)$$

with $\boldsymbol{l}$ being the angular momentum of the rim per unit length, in order to derive the moment-of-momentum-balance equation.

The moment-of-momentum equation for the rim is written relative to the centre of mass $\mathscr{G}$ of the element of the rim:

$$\boldsymbol{l}_{,t} + \lambda_{,t}\lambda^{-1}\boldsymbol{l} = \lambda^{-1}\boldsymbol{M}_{G,\zeta} + \boldsymbol{\tau} \times \boldsymbol{Q} + \rho h_S(1 - \kappa y'_S)[(\boldsymbol{u}_{SR} - \boldsymbol{V}) \cdot \boldsymbol{n}_S][\boldsymbol{x}_{GL} \times (\boldsymbol{u}_{SR} - \boldsymbol{V})], \quad (2.13)$$

where $\boldsymbol{M}_G$ is the momentum of the stresses relative to the centre of mass and $\boldsymbol{x}_{GL} = \boldsymbol{r}_S - \boldsymbol{r}_G$ is the coordinate of the mouth of the sheet entering the rim.

It can be shown that the rate of change of the angular momentum of the element of rim relative to $\mathscr{G}$ can be expressed with the help of (2.12) as

$$\begin{aligned}\boldsymbol{l}_{,t} &= \int_{\mathscr{S}} (1 - \kappa y')\boldsymbol{x}_G \times \{\boldsymbol{w}_{G,t} + 2\boldsymbol{\Omega} \times \boldsymbol{w}_G + \boldsymbol{\Omega} \times (\boldsymbol{\Omega} \times \boldsymbol{x}_G) + \boldsymbol{\Omega}_{,t} \times \boldsymbol{x}_G + \boldsymbol{X}_{G,tt}\}\rho\,\mathrm{d}\mathscr{S} \\ &= \int_{\mathscr{S}} (1 - \kappa y')\boldsymbol{x}_G \times \{\boldsymbol{w}_{G,t} + 2\boldsymbol{\Omega} \times \boldsymbol{w}_G\}\rho\,\mathrm{d}\mathscr{S} + \rho\boldsymbol{\Omega} \times (\boldsymbol{I}_G \cdot \boldsymbol{\Omega}_G) + \rho\boldsymbol{I}_G \cdot \boldsymbol{\Omega}_{,t}, \quad (2.14)\end{aligned}$$

where $\boldsymbol{X}_G = \boldsymbol{X}_R + \boldsymbol{r}_G$ is the radius vector of the centre of mass of the rim element, $\boldsymbol{x}_G = \boldsymbol{r} - \boldsymbol{r}_G$ is the radius vector with origin at point $\mathscr{G}$ and $\boldsymbol{w}_G = \boldsymbol{w} - \boldsymbol{r}_{G,t}$ is the velocity in the rim in the coordinate system fixed at point $\mathscr{G}$. The time derivatives $\boldsymbol{r}_{G,t}$ and $\boldsymbol{w}_{G,t}$ are taken in the accelerating and the rotating coordinate system fixed at $\mathscr{G}$. The term $\boldsymbol{I}_G\rho\lambda\,\mathrm{d}\zeta$ is the moment-of-inertia tensor of the element of rim, which is defined by

$$\boldsymbol{I}_G = \int_{\mathscr{S}} (1 - \kappa y')[(\boldsymbol{x}_G \cdot \boldsymbol{x}_G)\boldsymbol{1} - \boldsymbol{x}_G \otimes \boldsymbol{x}_G]\,\mathrm{d}\mathscr{S}, \quad (2.15)$$

where $\boldsymbol{1}$ is the unit tensor and the symbol $\otimes$ denotes the tensor product. Also note that the volume integral of $\boldsymbol{x}_G$ in the element of the rim vanishes due to the definition of the centre of mass.

2.3. *Components of the forces and moments of stresses applied to the rim cross-section*

Approximating the cross-section of the rim by a circle of radius $a(\zeta, t)$, it is natural to describe the stresses and the forces associated with the flow in the rim by the stresses which appear in a free circular cylinder of the same radius.

2.3.1. *Free viscous jet of a circular cross-section*

If the effect of the acceleration of the rim centreline on the shape of its cross-section is small, the internal stresses in the rim can be estimated from quasi-two-dimensional theory for the dynamics of a free circular liquid jet (Entov & Yarin 1984; Yarin 1993).

For the circular jet cross-section of radius a the diagonal components of the strain rate tensor $\boldsymbol{D}_J$ are obtained in the following form:

$$D_{J\tau\tau} = -2\delta\left(1 + \tfrac{3}{2}y'\kappa\right) - [z'(\tau\Omega_b - \lambda^{-1}\Omega_{n,\zeta} - \kappa\Omega_\tau) + y'(\lambda^{-1}\Omega_{b,\zeta} + \tau\Omega_n)], \quad (2.16a)$$

$$D_{Jnn} = D_{Jbb} = -\frac{D_{J\tau\tau}}{2}, \quad (2.16b)$$

where

$$\delta \equiv -\tfrac{1}{2}(\lambda^{-1}V_{\tau,\zeta} - \kappa V_n). \quad (2.16c)$$

Equation (2.16b) expresses the continuity condition.

The stresses in a Newtonian jet,

$$\boldsymbol{\sigma} = -p\boldsymbol{1} + 2\mu\boldsymbol{D}, \quad (2.17)$$

are then obtained from the boundary conditions at the jet surface:

$$\sigma_{Jnn} = \sigma_{Jbb} = -\sigma\left[H - \kappa a^{-1}y'(1 + \lambda^{-2}a_{,\zeta}^2)^{-3/2}\right], \quad (2.18a)$$

$$H \equiv a^{-1}\left(1 + \lambda^{-2}a_\zeta^2\right)^{-1/2} - \left(1 + \lambda^{-2}a_{,\zeta}^2\right)^{-3/2}\lambda^{-1}[\lambda^{-1}a_{,\zeta}]_{,\zeta}, \quad (2.18b)$$

where p is the pressure and H is the double mean curvature of the jet surface.

2.3.2. *Stresses in a rim*

In addition to the stresses associated with the jet stretching and bending, the stresses in the rim are also influenced by the flow generated by the flux entering the rim from the sheet. The volumetric flow rate of this flow per unit length of the rim is

$$W = h_{SR}(\boldsymbol{V} - \boldsymbol{u}_{SR}) \cdot \boldsymbol{n}_S(1 - \kappa y_S'). \quad (2.19)$$

This flow leads to additional growth of the rim radius a and the corresponding stresses are shear-free at the rim surface. In this study, in order to estimate these stresses, the linearized relative flow in the rim cross-section associated with the flow rate W is approximated by its radial expansion:

$$\boldsymbol{w}_W = \frac{W}{2\pi a^2}(y'\boldsymbol{n} + z'\boldsymbol{b}). \quad (2.20)$$

The corresponding average components of the strain rate tensor are

$$D_{Wnn} = D_{Wbb} = \frac{W}{2\pi a^2}, \quad D_{W\tau\tau} = 0. \quad (2.21)$$

Finally, the strain rate tensor in the rim is estimated by

$$\boldsymbol{D} = \boldsymbol{D}_J + \boldsymbol{D}_W. \quad (2.22)$$

Moreover, if we consider the rim dynamics, the terms associated with the velocity acceleration in the $\boldsymbol{n}$ and $\boldsymbol{b}$ directions are significant and cannot always be neglected. These terms do not appear in expressions (2.18a). Since the shear stresses in the rim and the inertial effects associated with the radial velocity relative to the rim axis are assumed to be small and thus neglected, we expect that

$$\frac{\partial\sigma_{nn}}{\partial y'} = -\rho\boldsymbol{V}_{,t} \cdot \boldsymbol{n}, \quad \frac{\partial\sigma_{bb}}{\partial z'} = -\rho\boldsymbol{V}_{,t} \cdot \boldsymbol{b}, \quad (2.23)$$

which is not consistent with expressions (2.18a). In fact, the gradients of the stresses in the rim initiated by the rim acceleration lead to the deformation of the rim cross-section. Therefore, expression (2.18a) is not applicable in such cases.

Note that if the Bond number,

$$Bo = \frac{\rho a^2}{\sigma}|\boldsymbol{V}_{,t} - (\boldsymbol{V}_{,t}\cdot\boldsymbol{\tau})\boldsymbol{\tau}|, \tag{2.24}$$

is small, the deformation of the rim cross-section is also negligibly small and its shape is well approximated by a circle, and the average pressure in the rim is not influenced significantly. Here the term $[\boldsymbol{V}_{,t} - (\boldsymbol{V}_{,t}\cdot\boldsymbol{\tau})\boldsymbol{\tau}]$ expresses the projection of the material acceleration on the plane $\{\boldsymbol{n}, \boldsymbol{b}\}$.

In this study, only the first-order approximations of the stresses in the rim are taken into account, which neglects the deformation of the rim cross-section:

$$\sigma_{nn} = \sigma_{bb} = \Sigma \equiv -\sigma H - \rho \boldsymbol{V}_{,t}\cdot(y'\boldsymbol{n} + z'\boldsymbol{b}). \tag{2.25}$$

The stresses in the $\boldsymbol{\tau}$ direction are determined using (2.16*b*), (2.17), (2.21) and (2.22) in the following form:

$$\sigma_{\tau\tau} = -\sigma H - \rho \boldsymbol{V}_{,t}\cdot(y'\boldsymbol{n} + z'\boldsymbol{b}) + 3\mu D_{J\tau\tau} - \frac{\mu W}{A}. \tag{2.26}$$

2.3.3. *Forces and moments of stresses applied to the rim cross-section*

The total longitudinal force $P\boldsymbol{\tau}$ applied to the jet cross-section consists of the force component associated with the internal stress $\sigma_{\tau\tau}$ and surface tension. It can be expressed in the form

$$P = \int_{\mathscr{S}} \sigma_{\tau\tau}\,\mathrm{d}\mathscr{S} + 2\pi\sigma a\left(1 + \lambda^{-2}a_{,\zeta}^2\right)^{-1/2}. \tag{2.27}$$

The expression for the force P applied to the rim of circular cross-section can then be derived from (2.27) using (2.25) and (2.26):

$$P = A\left[\sigma a^{-1}\left(1 + \lambda^{-2}a_{,\zeta}^2\right)^{-1/2} + \sigma\left(1 + \lambda^{-2}a_{,\zeta}^2\right)^{-3/2}\lambda^{-1}(\lambda^{-1}a_{,\zeta})_{,\zeta} - 6\mu\delta\right] - \mu W. \tag{2.28}$$

The moment of stresses $\boldsymbol{M}$ applied to the rim cross-section relative to the rim centreline is estimated from

$$\boldsymbol{M} \equiv \int_{\mathscr{S}} \sigma_{\tau\tau}(\boldsymbol{r}\times\boldsymbol{\tau})\,\mathrm{d}\mathscr{S} = \int_{\mathscr{S}} \sigma_{\tau\tau}(z'\boldsymbol{n} - y'\boldsymbol{b})\,\mathrm{d}\mathscr{S}. \tag{2.29}$$

The expression for $\boldsymbol{M}$ is obtained with the help of (2.25) and (2.26) in the following form:

$$M_n = 3\mu I(\lambda^{-1}\Omega_{n,\zeta} - \tau\Omega_b + \kappa\Omega_\tau) + \rho I(\boldsymbol{V}_{,t}\cdot\boldsymbol{b}), \tag{2.30a}$$

$$M_b = 3\mu I\left(\lambda^{-1}\Omega_{b,\zeta} + \tau\Omega_n + \tfrac{3}{2}\kappa\lambda^{-1}V_{\tau,\zeta} + \tfrac{3}{2}\kappa^2 V_n\right) - \rho I(\boldsymbol{V}_{,t}\cdot\boldsymbol{n}), \tag{2.30b}$$

where $I = I_b = I_n = \pi a^4/4$, $I_{bn} = 0$.

Finally, the moment of stresses relative to the centre of mass $\mathscr{G}$ is determined as

$$\boldsymbol{M}_G = \boldsymbol{M} - \boldsymbol{r}_G \times \boldsymbol{P}. \tag{2.31}$$

3. Linear stability analysis of an infinite, straight, viscous rim

Consider now a stationary Cartesian coordinate system $\{x, y, z\}$ with base unit vectors $\{\boldsymbol{e}_x, \boldsymbol{e}_y, \boldsymbol{e}_z\}$ and a rim bounding a thin planar liquid sheet of thickness $h_S(y,t)$ and velocity $V_S(y,t)$, whose median surface lies in the plane $\{x, y\}$, as shown in

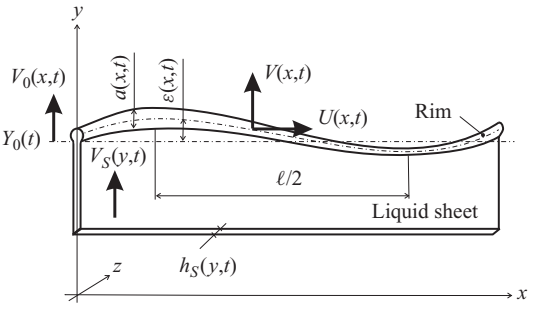

FIGURE 4. Sketch of the disturbed rim.

figure 4. Also consider a stretching S of the free sheet in the y direction defined as $S(y,t)=\partial V_S/\partial y$. The stretching leads to the emergence of viscous stresses in the sheet which then influence the dynamics of the rim. In this study, the effect of the rim formation on the film flow is assumed to be negligibly small, which is typical for low-viscosity fluids (Yarin 1993). The film stretching is therefore an independent parameter in our problem.

The stress tensor in a free, thin planar liquid sheet can be found (Yarin 1993) as

$$\boldsymbol{\sigma}_S = 2\mu[S\boldsymbol{e}_x \otimes \boldsymbol{e}_x + 2S\boldsymbol{e}_y \otimes \boldsymbol{e}_y], \tag{3.1}$$

using the condition of vanishing of the z component of the stress tensor.

3.1. *Base solution*

The base solution for the undisturbed rim was obtained by Taylor (1959*b*) and can also be found in Yarin (1993) and Roisman *et al.* (2006). Here it is written to account for the viscous stresses emerging in the liquid film:

$$\frac{\mathrm{d}Y_0(t)}{\mathrm{d}t} = V_0(t), \quad \frac{\mathrm{d}A_0(t)}{\mathrm{d}t} = [V_S(Y_0,t) - V_0(t)]h_S(Y_0,t), \tag{3.2a,b}$$

$$A_0(t)\frac{\mathrm{d}V_0(t)}{\mathrm{d}t} = [V_S(Y_0,t) - V_0(t)]^2 h_S(Y_0,t) - \frac{2\sigma}{\rho} - \frac{4\mu S h_S(Y_0,t)}{\rho}, \tag{3.2c}$$

where $Y_0(t)$ is the undisturbed position of the rim centreline, $A_0(t)$ is the rim cross-section area and V_0 is the rim transverse velocity. It can be shown that solution (3.2) satisfies the equations for rim dynamics derived in § 2.

3.2. *Long-wave approximation of a disturbed rim*

In order to analyse the stability of the rim we consider only small disturbances of the rim centreline $y=Y(x,t)$ and radius $a(x,t)$. For very small disturbances ($\partial Y/\partial x \ll 1$ and $\partial a/\partial x \ll 1$) the system of governing equations (2.9), (2.11) and (2.12) can be linearized and written in the coordinate system $\{x, y, z\}$. The transverse and longitudinal components of the liquid velocity in the disturbed rim are denoted as $V(x,t) \equiv \partial Y/\partial t$ and $U(x,t)$, respectively. The balance equations for the mass and momentum in the x and y directions and for the moment of momentum in the z direction are

$$\frac{\partial A}{\partial t} + \frac{\partial AU}{\partial x} - h_S(V_S - V)(1 + \kappa a_0) = 0, \tag{3.3a}$$

$$\rho A\frac{\partial U}{\partial t} - \frac{\partial P}{\partial x} + \rho h_S(V_S - V)U - 2\sigma\frac{\partial Y}{\partial x} = 0, \tag{3.3b}$$

$$\rho A\frac{\partial V}{\partial t}-P\kappa-\frac{\partial Q}{\partial x}+[2\sigma-\rho h_S(V_S-V)^2+4\mu Sh_S](1+\kappa a_0)=0, \tag{3.3c}$$

$$\rho\frac{\partial I_0\Omega}{\partial t}-\frac{\partial M}{\partial x}-Q+\rho h_S a_0(V_S-V_0)U=0, \tag{3.3d}$$

with the expressions for the forces and moments of stresses obtained with the help of (2.28) and (2.30) and approximate values for the curvature and the angular velocity with the help of (2.2) and (2.7):

$$P=\pi\sigma a+\sigma A_0\frac{\partial^2 a}{\partial x^2}+3\mu A\frac{\partial U}{\partial x}-\mu h_S(V_S-V)(1+\kappa a_0), \tag{3.4a}$$

$$M=-\rho I\frac{\partial V}{\partial t}+3\mu I_0\frac{\partial \Omega}{\partial x}+\frac{\kappa I_0}{A_0}P, \tag{3.4b}$$

$$\kappa=\frac{\partial^2 Y}{\partial x^2},\quad \Omega=\frac{\partial V}{\partial x}. \tag{3.4c,d}$$

The linearized balance equations (3.3) were obtained by Roisman *et al.* (2006) for the inviscid case whereas expressions (3.4*a*) and (3.4*b*) for the force and momentum applied to the rim cross-section include new terms associated with the viscous stresses.

Consider small disturbances of the rim centreline, of the radius of its cross-section and of its velocity of the form

$$Y=Y_0(t)+\epsilon(x,t),\quad a=a_0(t)+\alpha(x,t),\quad U=u(x,t). \tag{3.5}$$

The system of linearized equations for these small disturbances can now be obtained easily from (3.3):

$$2\pi a_0\alpha_{,t}+A_0u_{,x}+h(\epsilon_{,t}-S\epsilon)-W_0a_0\left(\epsilon_{,xx}-\alpha/a_0^2\right)=0, \tag{3.6a}$$

$$-\rho A_0u_{,t}+\pi\sigma\alpha_{,x}+\sigma A_0\alpha_{,xxx}+3\mu A_0u_{,xx}-\mu W_0a_0\epsilon_{,xxx}+\mu h_S(\epsilon_{,tx}-S\epsilon_{,x})-\rho W_0u+2\sigma\epsilon_{,x}=0, \tag{3.6b}$$

$$-\rho A_0\epsilon_{,tt}-\pi\rho a_0\dot V_0\left(2\alpha-a_0^2\epsilon_{,xx}\right)+\pi\sigma a_0\epsilon_{,xx}+\mu W_0\epsilon_{,xx}+Q_{,x}-2\rho W_0(\epsilon_{,t}-S\epsilon)=0, \tag{3.6c}$$

$$2\rho I_0\epsilon_{,xtt}+\rho\dot I_0\epsilon_{,xt}+\pi\rho a_0^3\dot V_0\alpha_{,x}-3\mu I_0\epsilon_{,xxxt}-\frac{\pi\sigma a_0^3}{4}\epsilon_{,xxx}+\rho a_0W_0u-Q+\frac{a_0^2}{4}\mu W_0\epsilon_{,xxx}=0, \tag{3.6d}$$

where

$$W_0=h(V_{S0}-V_{R0}),\quad \dot I_0\equiv\frac{\mathrm{d}I_0}{\mathrm{d}t}=\frac{a_0^2W_0}{2},\quad \dot V_0\equiv\frac{\mathrm{d}V_0}{\mathrm{d}t}, \tag{3.7}$$

with W_0 being the volumetric flow rate per unit length of the liquid entering the rim.

3.3. *Immediate loss of stability*

Coefficients a_0, A_0 and I_0 are functions of time and the exact solution of the system of equations (3.6) is not trivial. Nevertheless, an expected fast exponential growth of the rim disturbance in the case of its instability allows one to be obtained for a standard linear stability analysis with 'frozen' parameters a_0, A_0 and I_0.

Assume small rim disturbances of the form

$$\epsilon=\epsilon_0\exp(\omega t+\mathrm{i}\xi x),\quad \alpha=\alpha_0\exp(\omega t+\mathrm{i}\xi x), \tag{3.8a,b}$$

$$u=u_0\exp(\omega t+\mathrm{i}\xi x),\quad Q=q_0\exp(\omega t+\mathrm{i}\xi x), \tag{3.8c,d}$$

where ω is the growth rate of the disturbances and $\xi = 2\pi/\ell$ is the wavenumber (ℓ being the disturbance wavelength).

The linearized system (3.6) can now be reduced to the following form:

$$\boldsymbol{A} \cdot \boldsymbol{b} = 0, \tag{3.9}$$

where

$$\boldsymbol{A} = \begin{pmatrix} 2\pi a_0\omega + W_0/a_0 & A_0 \mathrm{i}\xi & A_{13} & 0 \\ \pi\sigma \mathrm{i}\xi - \sigma A_0 \mathrm{i}\xi^3 & A_{22} & A_{23} & 0 \\ -2\pi\rho a_0 \dot{V}_0 & 0 & A_{33} & \mathrm{i}\xi \\ \pi\rho a_0^3 \dot{V}_0 \mathrm{i}\xi & \rho a_0 W_0 & A_{43} & -1 \end{pmatrix}, \tag{3.10a}$$

$$\boldsymbol{b} = (\alpha_0 \quad u_0 \quad \epsilon_0, \quad q_0)^{\mathrm{T}}, \tag{3.10b}$$

$$A_{13} = h(\omega - S) + a_0 W_0 \xi^2, \tag{3.10c}$$

$$A_{22} = -\rho W_0 - \rho A_0 \omega - 3A_0 \mu \xi^2, \tag{3.10d}$$

$$A_{23} = \mu W_0 a_0 \mathrm{i}\xi^3 + \mu h \mathrm{i}\xi(\omega - S) + 2\sigma \mathrm{i}\xi, \tag{3.10e}$$

$$A_{33} = -\rho A_0 \omega^2 - 2\rho W_0(\omega - S) - \left(\pi\rho a_0^3 \dot{V}_0 + \mu W_0 + \pi\sigma a_0\right)\xi^2, \tag{3.10f}$$

$$A_{43} = 2\rho I_0 \omega^2 \mathrm{i}\xi + \frac{\rho a_0^2 W_0}{2}\omega \mathrm{i}\xi + 3I_0 \mu\, \omega \mathrm{i}\xi^3 + \frac{\pi a_0^3 \sigma - \mu W_0 a_0^2}{4}\mathrm{i}\xi^3. \tag{3.10g}$$

The dispersion relation corresponding to (3.6) is obtained as

$$C_4 \overline{\omega}^4 + C_3 \pi \overline{\omega}^3 + C_2 \overline{\omega}^2 + C_1 \overline{\omega} + C_0 = 0, \tag{3.11}$$

where the coefficients C_0, C_1, C_2, C_3 and C_4 are functions of the dimensionless parameters of the problem. Obtaining expressions for these parameters is a straightforward algebraic operation but they are rather long and as such are omitted. All the overbarred variables and parameters starting from (3.11) are dimensionless, with $\sqrt{\rho a_0^3/\sigma}$ taken as the time scale and a_0 as the length scale.

The main parameters of the problem are expressed through the dimensionless variables as

$$\left.\begin{aligned} &\omega = \sqrt{\frac{\sigma}{\rho a_0^3}}\,\overline{\omega}, \qquad S = \sqrt{\frac{\sigma}{\rho a_0^3}}\,\overline{S}, \qquad \dot{V}_0 = \frac{\sigma}{\rho a_0^2}\overline{\dot{V}}_0, \\ &\xi = \overline{\xi}/a_0, \qquad h_S = \overline{h} a_0, \qquad W_0 = \overline{W}_0 \sqrt{\frac{\sigma a_0}{\rho}}. \end{aligned}\right\} \tag{3.12}$$

The relation between $\overline{W}_0$ and $\overline{\dot{V}_0}$ can be found from the base solution (3.2):

$$\overline{W}_0 = \sqrt{\overline{h}(2 + \pi\overline{\dot{V}_0} + 4\overline{h}Oh\overline{S})}. \tag{3.13}$$

The dispersion relation (3.11) is an algebraic equation for $\overline{\omega}$ and has four roots. The appearance of a root with a positive real part indicates instability of the rim.

The rim acceleration $\mathrm{d}V_0/\mathrm{d}t$ can be calculated from (3.2*c*) at any instant of time. For a given flow in the film, its value is determined by the initial conditions and by the history of the rim propagation. The acceleration does not vanish even if at some instant of time, the velocity gradient in the film is zero. Therefore, in our analysis, $\mathrm{d}V_0/\mathrm{d}t$ is considered as an independent parameter.

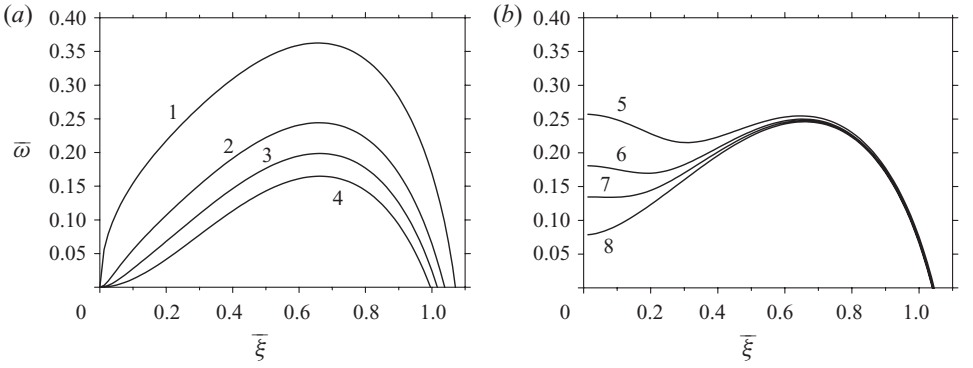

FIGURE 5. Dimensionless rate of growth of the rim disturbances as a function of the wavenumber. $Oh = 0.1$ and $\overline{V}_0 = -0.1$. (*a*) $\overline{S} = 0$ and the film thickness varies (line 1, $\overline{h} = 0$; line 2, $\overline{h} = 0.1$; line 3, $\overline{h} = 0.2$; line 4, $\overline{h} = 0.3$); (*b*) $\overline{h} = 0.1$ and the film stretching varies (line 5, $\overline{S} = 0.5$; line 6, $\overline{S} = 0.3$; line 7, $\overline{S} = 0.2$; line 8, $\overline{S} = 0.1$).

4. Results and discussion

4.1. *Rate of growth of the linear rim disturbances*

Values of the maximum positive root of (3.11) are shown in figure 5 as a function of the wavelength $\overline{\xi}$ for various parameters. The value of $\overline{\omega}$ is positive at small values of the wavenumber and reaches a maximum at $\overline{\xi} \approx 0.6 - 0.8$, which is of the same order as the wavelength of the most dangerous mode of the capillary instability of a free cylindrical jet (Rayleigh 1879). In figure 5(*a*) the effect of the film thickness is investigated. In figure 5(*b*) values for $\overline{\omega}$ are shown at various values of the dimensionless film stretching $\overline{S}$. In the range of $\overline{S}$ considered, film stretching has almost no influence on the maximum growth rate $\overline{\omega}$ at wavenumbers $\overline{\xi} > 0.5$, whereas the growth rates of the longest waves (with $\overline{\xi} < 0.3$) increase significantly. This means that in the presence of film stretching, relatively stable long parts of the rim can appear. Such long parts of the rim have been reported in Roisman *et al.* (2007), where they have also been predicted theoretically for an inviscid rim.

Using the dispersion relation (3.11), it is possible to calculate the maximum growth rate of the rim disturbances $\overline{\omega}_*$ and the corresponding wavenumber $\overline{\xi}_*$. The values of $\overline{\omega}_*$ are shown in figure 6 for various parameters. In all cases, rim deceleration leads to a significant increase of $\overline{\omega}_*$ whereas viscosity and a larger relative film thickness stabilize the rim. The result is in agreement with the evident stabilizing role of viscosity (Weber 1931).

The values of the dimensionless wavelength $\overline{\ell}_* = 2\pi/\overline{\xi}_*$ of the most unstable mode are shown in figure 7. In all cases, the variation of $\overline{\ell}_*$ is relatively small and remains in the range $8 < \overline{\ell} < 11$ for a wide range of the parameters used in the analysis. Rim deceleration leads to some small decrease in the value of $\overline{\ell}_*$ whereas viscosity leads to some increase of $\overline{\ell}_*$.

This result is confirmed by experimental data for the relative distance between the jets emerging from the rim due to its instability. These distances can be estimated easily from the images of splash produced by a single-drop impact (Yarin & Weiss 1995; Cossali *et al.* 2004; Vander Wal, Berger & Mozes 2005; Roisman *et al.* 2006) and of spray impact (Roisman *et al.* 2007). In most of the cases, the inter-jet distance is approximately 10 rim radii.

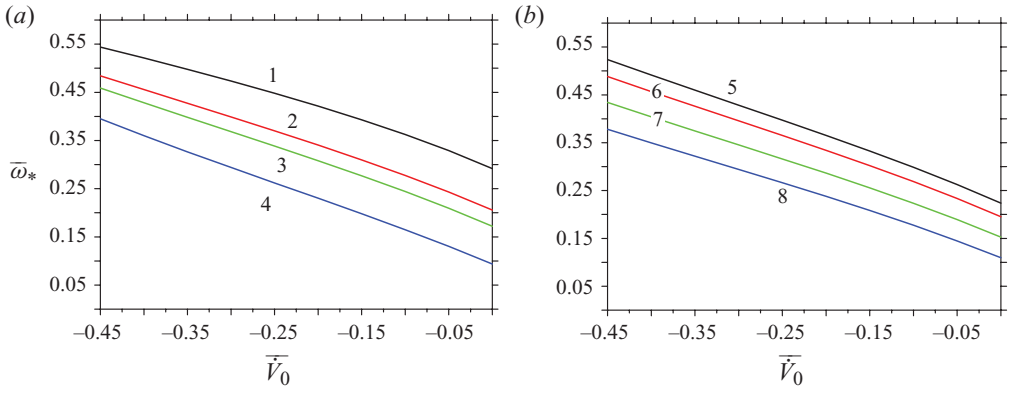

FIGURE 6. (Colour online) Maximum growth rate as a function of the rim acceleration at various parameters, $\overline{S}=0$. (*a*) Effect of the film thickness at $Oh=0.1$ (line 1, $\overline{h}=0$; line 2, $\overline{h}=0.05$; line 3, $\overline{h}=0.1$; line 4, $\overline{h}=0.3$) and (*b*) effect of the Ohnesorge number at $\overline{h}=0.1$ (line 5, $Oh=0$; line 6, $Oh=0.05$; line 7, $Oh=0.15$; line 8, $Oh=0.3$).

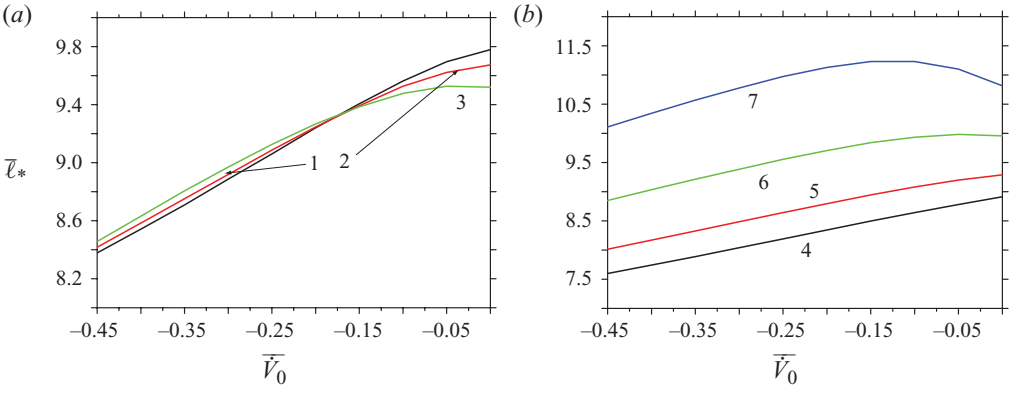

FIGURE 7. (Colour online) Most unstable wavelength $\overline{\ell}_*$ as a function of the rim acceleration, $\overline{S}=0$. (*a*) Effect of the dimensionless film thickness at $Oh=0.1$ (line 1, $\overline{h}=0$; line 2, $\overline{h}=0.1$; line 3, $\overline{h}=0.3$) and (*b*) effect of the Ohnesorge number at $\overline{h}=0.1$ (line 4, $Oh=0$; line 5, $Oh=0.05$; line 6, $Oh=0.15$; line 7, $Oh=0.3$).

An interesting question related to the stability analysis is: What is the shape of the deformed rim? To answer this question, the eigenvector of the system (3.6) is determined, which allows us to predict the ratios of the amplitudes ϵ_0/α_0 and u_0/α_0. The value of ϵ_0/α_0 is dimensionless whereas the ratio u_0/α_0 can be scaled using

$$\frac{u_0}{\alpha_0}=\mathrm{i}\sqrt{\frac{\sigma}{\rho a_0^3}}\frac{\overline{u}_0}{\overline{\alpha}_0}. \tag{4.1}$$

The imaginary unit i appears in (4.1) to ensure real values of the ratio $\overline{u}_0/\overline{\alpha}_0$.

In figure 8 the dimensionless amplitude ratios $\overline{u}_0/\overline{\alpha}_0$ and ϵ_0/α_0 at the maximum growing mode (corresponding to ω_* and ξ_*) are shown as functions of the dimensionless rim acceleration $\dot{\overline{V}}_0$. Variation of various other parameters of the problem leads to only minor changes in the predicted values of $\overline{u}_0/\overline{\alpha}_0$ and ϵ_0/α_0. The Ohnesorge number has a notable effect on the ratio ϵ_0/α_0.

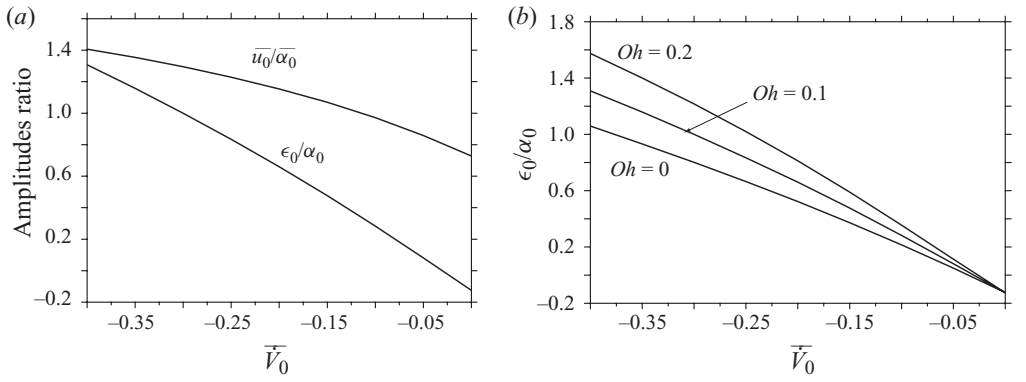

FIGURE 8. Ratios of the dimensionless amplitudes $\overline{u}_0/\overline{\alpha}_0$ and ϵ_0/α_0 of the eigenvector of the system as a function of the rim acceleration, $\overline{S} = 0.1$ and $\overline{h} = 0.1$. (*a*) The velocity u_0 and the rim deflection ϵ_0 amplitudes normalized by the disturbances of the rim radius α_0 at $Oh = 0.1$ and (*b*) ratio ϵ_0/α_0 at various Ohnesorge numbers.

4.2. *Distance between finger-like jets*

One of the further parameters which can be used for theory validation is the distance between the finger-like jets appearing due to rim instability.

It is not trivial to design a validating experiment in which the flow in the sheet and in a nearly straight rim will be perfectly controlled. In order to observe the initial stages of the rim instability and measure its typical wavelength and growth rate, an axisymmetric spreading of a free sheet resulting from jet or drop collision with a rigid impactor could be considered best. Such collisions have been investigated in Clanet & Villermaux (2002) and Rozhkov *et al.* (2002). In the case of the radial expansion of the rim centreline, additional stresses appear in the rim cross-section associated with $\mu V_n \kappa$. They vanish in the case of the nearly straight rim considered in the present study.

Moreover, the inter-jet distances in the experiments may not be necessarily exactly equal to the most unstable wavelength since their values are influenced by the spectrum of the initial natural disturbances.

On the other hand, high-speed video observations of spray impact (several sequences of which are shown in figure 1) provide a large number of data which can then be analysed. Some of the results of the measurements of the inter-jet distances in a water spray have been presented in Roisman *et al.* (2007). The spray is generated by a full-cone pressure-swirl atomizer. The volumetric flux is varied from 0.25 to 0.5 $\mathrm{l\,min^{-1}}$. The average drop velocity is in the range 5–11 $\mathrm{m\,s^{-1}}$. It is interesting to analyse such data in more detail. In figure 9 the probability density function of the distribution of the dimensionless inter-jet distances $\overline{\ell} = 2\ell/D_{rim}$ is shown for rim diameters between 70 and 100 μm. Each point in the histogram is obtained by counting the values of $\overline{\ell}$ from the interval $\Delta\overline{\ell} = \pm 1$. The histogram is then normalized to obtain the probability density function.

Several peaks in the probability density function can be identified easily, which indicates that the mechanism of rim breakup is rather complicated. These peaks are clearly marked in figure 9.

In figure 10 the values of $2\ell/D_{rim}$ corresponding to the first two peaks are shown as a function of the diameter class of the rim. In most of the cases, the most probable inter-jet distance is comparable with the theoretically predicted values shown in

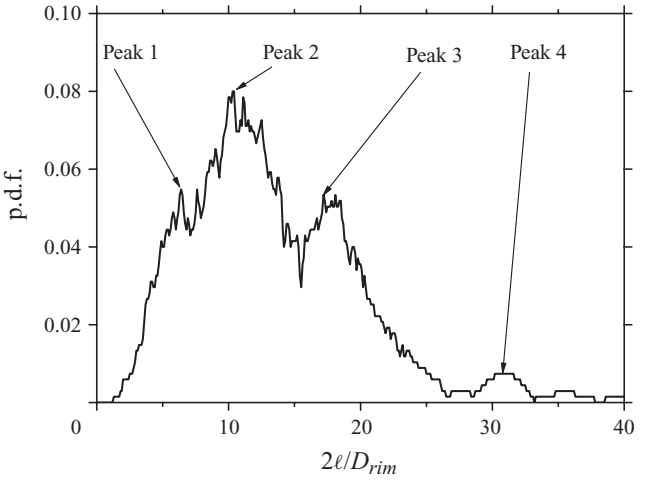

FIGURE 9. Probability density function (p.d.f.) of the distribution of the dimensionless inter-jet distances $2\ell/D_{rim}$ for the rim diameters between 70 and 100 μm.

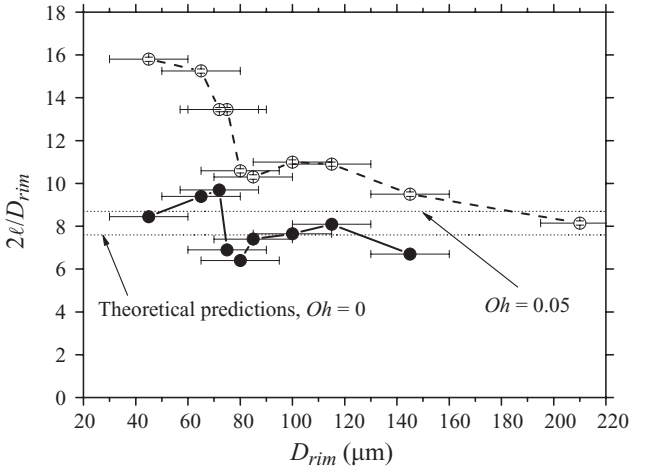

FIGURE 10. Spray impact onto a rigid wall. Most probable dimensionless inter-jet distances as a function of the rim diameter. The Ohnesorge number is in the range from $Oh = 0.01$ to $Oh = 0.03$. The theoretically predicted values for the inter-jet distances range from $2\ell/D_{rim} = 7.6$ (at $Oh = 0$, $\bar{V}_0 = -0.4$) to $2\ell/D_{rim} = 8.7$ (at $Oh = 0.05$, $\bar{V}_0 = 0$) corresponding to lines 4 and 5 in figure 7(*b*). The error bars are defined by the corresponding class intervals for D_{rim} and $2\ell/D_{rim}$.

figure 7. The Ohnesorge number is in the range from 0.01 to 0.03. Therefore, the effect of viscosity on the rim instability in these experiments is negligibly small. For smaller rim diameter, the experimental values of $\bar{\ell}$ corresponding to the second peak increase and approach the theoretical value of the double wavelength of the most unstable mode, $\bar{\ell} \sim 2\bar{\ell}_*$.

In the case of spray impact, the initial disturbances are not uniform along the rim due to the interactions with other drops and with drop interactions with the fluctuating liquid film created on the substrate by spray impact. Therefore, the finger-like jets do not appear from the rim simultaneously. Some of the inter-jet distances

thus correspond to the multiple length of the most unstable wave. Moreover, the resolution of the camera is 20 μm, which is comparable with the smallest rim diameters shown in figure 10. In the case of such small rim diameters, some bumps cannot be clearly identifiable, which also leads to statistically larger inter-jet distances.

Other possible reasons for some deviation of $\overline{\ell}$ from its theoretically predicted values is due to nonstationary effects, rim stretching and compression during breakup. However, it is obvious that the predicted values are of the same order of magnitude as the measured values of $\overline{\ell}$.

4.3. *Role of the moment-of-momentum equation*

It is obvious that in the absence of the rim acceleration and in the absence of the moment of momentum of the flow entering the rim, the capillary forces stabilize the rim bending. In this case the equation for the centreline bending (3.6*c*) is independent of the disturbances of the rim radius. It can be shown that the rim centreline is stable for all the other parameters of the problem. Our stability analysis, which accounts for the moment of momentum, shows that in the absence of acceleration, $\dot{\overline{V}}_0 \ll 1$, the amplitude of the rim bending does not vanish, but it is much smaller than the amplitude of the rim radius, $\epsilon_0/\alpha_0 \ll 1$. Therefore, in this regime the bending of the rim can be neglected and it deforms almost axisymmetrically. The mechanism of this deformation is explained by the Rayleigh capillary instability of a free infinite cylindrical jet. This result also indicates that the effect of the terms associated with the moment of momentum is also rather small. Our calculations show that it is small for various sets of problem parameters.

In this paper, much effort has been made in order to derive the moment-of-momentum equation of the rim. This equation can be significant if the components of the rim angular velocities, defined in (2.7), are high. The significance of this equation for rim stability was not known *a priori*. At this stage we can conclude that the moment of momentum does not determine the rim instability and its role is negligibly small. It will thus not be considered in the nonlinear simulations of rim propagation.

4.4. *Nonlinear rim deformation*

Consider as an example a rim bounding a uniform stretching film with a uniform velocity gradient $S(t)$ in the y direction. The dimensionless nonlinear equations of motion of the rim in the plane $\{x, y\}$ can be obtained from the mass and momentum-balance equations in the x and y directions, derived from (2.9) and (2.11) and written in Eulerian form:

$$(\lambda A)_{,t} + (\lambda A U)_{,x} = h_S(V_S - Y_{,t})(1 + \kappa a), \tag{4.2a}$$

$$\rho\lambda A(U_{,t} + UU_{,x}) = (\lambda^{-1}P)_{,x} + [2\sigma Y_{,x} + 2\mu h_S S - U h_S(V_S - Y_{,t})](1 + \kappa a), \tag{4.2b}$$

$$\rho\lambda A(V_{,t} + UV_{,x}) = [\rho h_S(V_S - Y_{,t})(V_S - V) - 2\sigma - 4\mu S h_S](1 + \kappa a), \tag{4.2c}$$

where the liquid velocity $V(x, t)$ in the y direction, the term $\lambda(x, t)$ and the curvature $\kappa(x, t)$ are defined as

$$V = Y_{,t} + UY_{,x}, \quad \lambda = \sqrt{1 + Y_{,x}^2}, \quad \kappa = \lambda^{-3}Y_{,xx}. \tag{4.2d}$$

The longitudinal and the normal velocities in the rim can be written as

$$V_n = \lambda^{-1}Y_{,t}, \quad V_\tau = \lambda U + \lambda^{-1}Y_{,x}Y_{,t}. \tag{4.3}$$

The stretching force P applied to the rim cross-section is defined in (2.28) with

$$\delta = -\tfrac{1}{2}(\lambda^{-1}V_{\tau,x} - \kappa V_n), \quad W = h_S(V_S - Y_{,t})(1 + \kappa a). \tag{4.4}$$

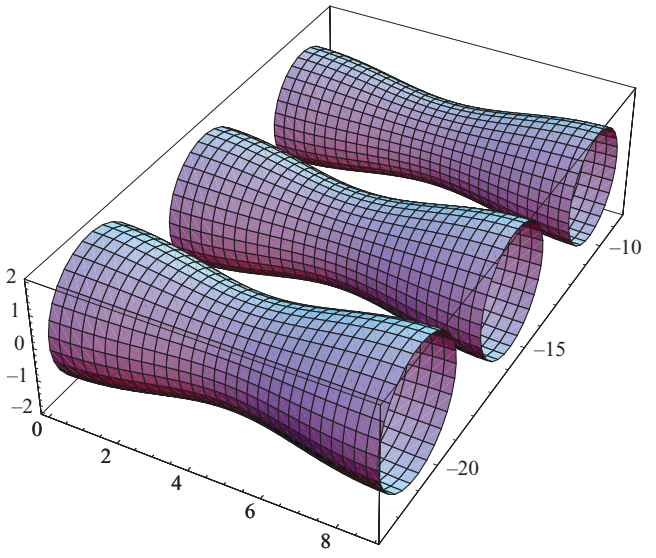

FIGURE 11. (Colour online) Nonlinear rim deformation. The film is stationary: $t \to \infty$, $V_S = 0$, $S = 0$ and $h_S = 0.3a_0$. The initial rim radius is $a = a_0[1 + 0.2\cos(\xi^* x)]$ and the initial velocity of the rim centreline is $Y_{,t} = -\sqrt{2\sigma/(\rho h_0)}$, where $\xi^* = 1/(\sqrt{2}a_0)$. The initial shape of the rim centreline is undisturbed. The Ohnesorge number is $Oh = 0.01$. The time instants are $4\times$, $6\times$ and $8\times\sqrt{\rho a_0^3/\sigma}$. The axis labels are dimensionless, scaled by the initial average rim radius a_0.

The velocity V_S and the thickness h_S of a free-stretching liquid film with a uniform velocity gradient can be obtained easily from the mass and momentum-balance equations:

$$V_S = \frac{Y}{t + t_0}, \quad h_S = \frac{h_{S0}t_0}{t_0 + t}, \quad S = \frac{1}{t + t_0}, \tag{4.5}$$

where t_0 is a parameter and h_{S0} is the initial film thickness.

The results of numerical integration of the system (4.2) are shown in figures 11–14. The boundary conditions are periodic at $x = 0$ and $x = 2a_0\pi/\xi^*$, where $\xi^* = 1/(\sqrt{2}a_0)$ is the wavelength of the most unstable mode of an inviscid infinite cylindrical jet. In figures 11 and 12 the evolution of the rim position and shape at several time instants is shown for the case of a stationary free film. Figure 11 shows the effect of the initial disturbance of the radius of the rim cross-section whereas figure 12 shows the influence of the initial disturbance of the rim centreline. In both cases the capillary forces stabilize the rim bending. The rim cross-section deforms solely due to the Rayleigh capillary instability. This result is in agreement with the CFD calculations of Fullana & Zaleski (1999).

In figure 13 the effect of relatively weak film stretching leading to rim acceleration is shown. This situation is relevant to the flow in the ejecta sheets produced by drop impact onto a liquid film (Thoroddsen 2002; Josserand & Zaleski 2003). The velocity gradient in such sheets appears due to the deceleration of the velocity of propagation of the base of the crown (Roisman & Tropea 2002). The disturbances of the rim centreline and of the rim radius, shown in figure 13, grow rather quickly, leading to the appearance of bulbous regions frequently observed during the initial stage of splashes caused by drop impact (figure 2).

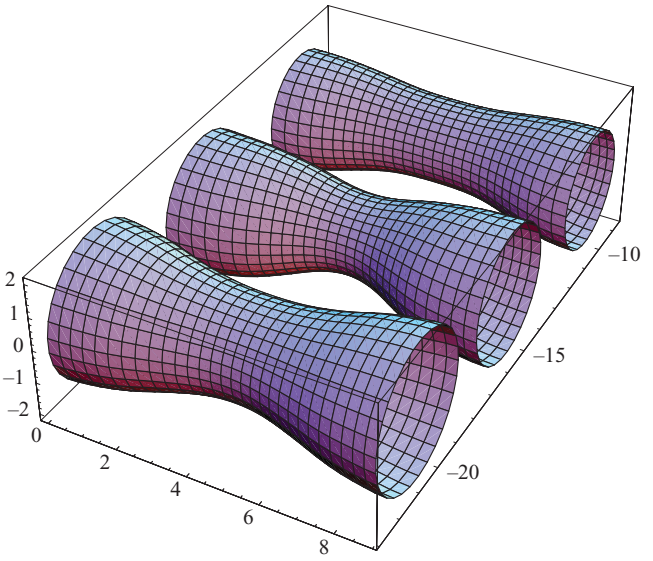

FIGURE 12. (Colour online) Nonlinear rim deformation. The film is stationary: $t \to \infty$, $V_S = 0$, $S = 0$ and $h_S = 0.3a_0$. The initial rim radius is undisturbed ($a = a_0$) and the initial velocity of the rim centreline is $Y_{,t} = -\sqrt{2\sigma/(\rho h_0)}$. The initial shape of the rim centreline is $Y = 0.5a_0 \cos(\xi^* x)$, where $\xi^* = 1/(\sqrt{2}a_0)$. The Ohnesorge number is $Oh = 0.01$. The time instants are $4\times$, $6\times$ and $8 \times \sqrt{\rho a_0^3/\sigma}$. The axis labels are dimensionless, scaled by the initial average rim radius a_0.

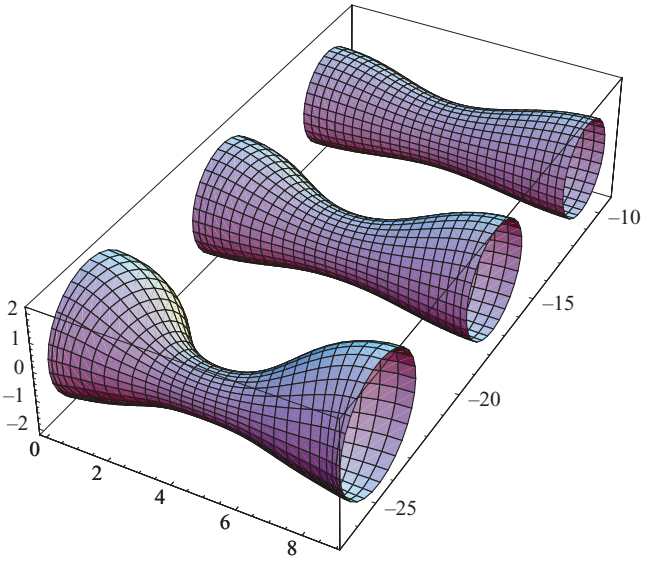

FIGURE 13. (Colour online) Nonlinear rim deformation and effect of the film stretching leading to the rim acceleration: $t_0 = 10\sqrt{\rho a_0^3/\sigma}$ and $h_0 = 0.3a_0$. The initial rim radius is $a = a_0[1 + 0.2\cos(\xi^* x)]$ and the initial velocity of the rim centreline is $Y_{,t} = -\sqrt{2\sigma/(\rho h_0)}$, where $\xi^* = 1/(\sqrt{2}a_0)$. The initial shape of the rim centreline is undisturbed. The Ohnesorge number is $Oh = 0.01$. The time instants are $4\times$, $6\times$ and $8 \times \sqrt{\rho a_0^3/\sigma}$. The axis labels are dimensionless, scaled by the initial average rim radius a_0.

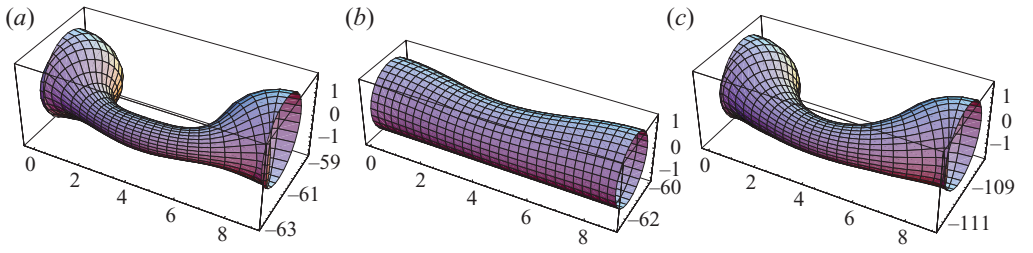

FIGURE 14. (Colour online) Nonlinear rim deformation and effect of the film stretching leading to the rim acceleration: $t_0 = 2\sqrt{\rho a_0^3/\sigma}$ and $h_0 = 0.1a_0$. The initial rim radius is $a = a_0[1 + 0.01\cos(\xi^* x)]$, the initial shape of the rim centreline is $Y = 0.005a_0\cos(\xi^* x)]$, the initial axial velocity distribution is $U = -0.01\sqrt{\sigma/(\rho a_0)}\sin(\xi^* x)]$ and the initial velocity of the rim centreline is $Y_{,t} = -\sqrt{2\sigma/(\rho h_0)}$, where $\xi^* = 1/(\sqrt{2}a_0)$. The axis labels are dimensionless, scaled by the initial average rim radius a_0. (*a*) $Oh = 0.01$ and $t = 9.5\sqrt{\rho a_0^3/\sigma}$; (*b*) $Oh = 0.5$ and $t = 9.5\sqrt{\rho a_0^3/\sigma}$; (*c*) $Oh = 0.5$ and $t = 14.5\sqrt{\rho a_0^3/\sigma}$.

The rim shown in figure 14 corresponds to stronger film stretching than in the case of figure 13. The initial disturbances of the rim radius are relatively small, $0.01a_0$, while the initial disturbances of the rim centreline and of the axial velocity are in the range obtained from the linear stability analysis (figure 8). The case shown in figure 14(*b*) corresponds to the same problem parameters as in figure 14(*a*) except for a much higher Ohnesorge number, $Oh = 0.5$. Viscosity leads to the decreasing of the rate of growth of instability but cannot prevent it, as shown in figure 14(*c*) for longer time.

4.5. *When the circular rim does not appear*

The conditions at the free edge of a free liquid sheet do not always lead to the formation of the rim of nearly circular cross-section, considered in this paper. The deformation of the rim by the viscous stresses becomes significant if they are comparable with the capillary pressure. The ratio of the viscous to the capillary stresses is described by the Ohnesorge number. Therefore, the analysis presented in this paper is valid only for the cases when $Oh \ll 1$ (Savva & Bush 2009).

Moreover, a rim is not formed if the viscous stresses in the film are balanced by the surface tension. The normal stress component in the free film in the planar case considered in this study is $\sigma_{Syy} = 4\mu S$ (see (3.1)). The critical-velocity gradient in the sheet at which a rim will not be formed can be easily obtained from the force balance $\sigma_{Syy}h + 2\sigma = 0$. This critical-velocity gradient can thus be estimated from $S_* = -\sigma/(\mu h)$.

Several examples of film flow not followed by rim formation can be found in Debrégeas, Martin & Brochard-Wyart (1995) and Roth *et al.* (2005). These studies are devoted to the investigation of hole growth in thin, very viscous free films. The Ohnesorge number in these studies is of the order of $Oh \sim 10^3$, far outside the range of validity of the present theory. The rate of hole growth in Debrégeas *et al.* (1995) and Roth *et al.* (2005) is estimated using an energy balance. This solution can, however, also be obtained considering force balance at the hole surface. The axisymmetric creeping flow in the viscous film is $\boldsymbol{v} = (\dot{R}R/r)\boldsymbol{e}_r$, where R is the radius of the hole, r is the radial coordinate in the film plane and $\boldsymbol{e}_r$ is the unit vector in the radial

direction. The stress tensor in this flow field is

$$\sigma_{rr} = -p - 2\mu\frac{\dot{R}R}{r^2}, \quad \sigma_{\phi\phi} = -p + 2\mu\frac{\dot{R}R}{r^2}, \quad \sigma_{zz} = -p, \tag{4.6}$$

where p is the pressure in the film.

Since the axial stress at the film surface vanishes (thus, $p = 0$), the expression for radial stress at the hole surface $r = R$ can be obtained in the form $\sigma_{rr} = -2\mu\dot{R}/R$. The force balance at the hole surface ($\sigma_{rr}h + 2\sigma = 0$) immediately yields the differential equation for the hole radius:

$$-\mu\frac{\dot{R}h}{R} + \sigma = 0. \tag{4.7}$$

The solution of this equation is $R = R_0 \exp[\sigma t/(\mu h)]$, where R_0 is the initial hole radius. Such exponential film growth has been observed in the experiments of Debrégeas *et al.* (1995) and Roth *et al.* (2005). As we see, flows at very high Ohnesorge numbers can be modelled without description of the rim propagation. Our theory of rim dynamics is therefore not applicable to such flows.

5. Conclusions

The governing equations for the evolution of a rim emerging at the edges of a thin viscous liquid sheet are derived from the mass, momentum and moment-of-momentum-balance equations. The resulting generalized theory accounts for inertial effects, capillary forces and viscous stresses in the rim and in the sheet.

The theory is used to investigate the stability of a straight viscous rim. The small axisymmetric disturbances of the rim radius, the antisymmetric disturbances of the rim centreline in the plane of the sheet and the small disturbances of the axial velocity of the liquid are all considered. The corresponding dispersion relation is obtained and solved for various parameters of the problem: the Ohnesorge number, the dimensionless rim acceleration, the relative film thickness and the dimensionless film stretching. The predicted wavelength of the most unstable mode is found to be very similar to the corresponding length obtained for a free infinite circular jet (Rayleigh 1879; Weber 1931) for a wide range of parameters. This length increases only slightly at higher Ohnesorge number.

It is shown that rim acceleration is one of the most significant influencing factors on the growth rate of the rim bending disturbances. Nonlinear numerical calculations demonstrate that the rim disturbances can lead to the formation of bulbous regions along the rim, which potentially lead to the generation of the finger-like jets frequently observed in experiments. The rim bounding a stationary uniform liquid film propagates with a constant velocity. The rim centreline in this case is stable.

This work was supported by the Deutsche Forschungsgemeinschaft (DFG) through grant no. 52100658 in the framework of Collaborative Research Centre SFB 568 (TP A1).

REFERENCES

Ashgriz, N. & Poo, J. Y. 1990 Coalescence and separation in binary collision of liquid drops. *J. Fluid Mech.* **221**, 183–204.

Bagué, A., Zaleski, S. & Josserand, C. 2007 Droplet formation at the edge of a liquid sheet. In *Proceedings of the Sixth International Conference on Multiphase Flow (ICMF 2007)* (ed. M. Sommerfeld & C. Tropea), Leipzig, Germany. ICMF.

Bartolo, D., Josserand, C. & Bonn, D. 2005 Retraction dynamics of aqueous drops upon impact on non-wetting surfaces. *J. Fluid Mech.* **545**, 329–338.

Boussinesq, J. 1869*a* Théories des expériences de Savart, sur la forme que prend une veine liquide après s'être choquée contre un plan circulaire. *C. R. Acad. Sci. Paris* **69**, 45–48.

Boussinesq, J. 1869*b* Théories des expériences de Savart, sur la forme que prend une veine liquide après s'être choquée contre un plan circulaire (suite). *C. R. Acad. Sci. Paris* **69**, 128–131.

Brenn, G., Valkovska, D. & Danov, K. D. 2001 The formation of satellite droplets by unstable binary drop collisions. *Phys. Fluids* **13**, 2463.

Brenner, M. P., Lister, J. R. & Stone, H. A. 1996 Pinching threads, singularities and the number 0.0304. . . . *Phys. Fluids* **8**, 2827–2836.

Brochard-Wyart, F. & De Gennes, P.-G. 1997 Shocks in an inertial dewetting process. *C. R. Acad. Sci. Paris* IIb **324**, 257–260.

Brochard-Wyart, F., Di Meglio, J. M. & Quéré, D. 1987 Dewetting: growth of dry regions from a film covering a flat solid or a fiber. *C. R. Acad. Sci. Paris* II **304**, 553–558.

Bush, J. W. M. & Hasha, A. E. 2004 On the collision of laminar jets: fluid chains and fishbones. *J. Fluid Mech.* **511**, 285–310.

Clanet, C. 2001 Dynamics and stability of water bells. *J. Fluid Mech.* **430**, 111–147.

Clanet, C. & Villermaux, E. 2002 Life of a smooth liquid sheet. *J. Fluid Mech.* **462**, 307–340.

Clark, C. J. & Dombrowski, N. 1972 On the formation of drops from the rims of fan spray sheets. *J. Aerosol. Sci.* **3** (3), 173–183.

Cossali, G. E., Marengo, M., Coghe, A. & Zhdanov, S. 2004 The role of time in single drop splash on thin film. *Exp. Fluids* **36**, 888–900.

Culick, F. E. C. 1960 Comments on a ruptured soap film. *J. Appl. Phys.* **31**, 1128–1129.

Debrégeas, G., Martin, P. & Brochard-Wyart, F. 1995 Viscous bursting of suspended films. *Phys. Rev. Lett.* **75**, 3886–3889.

Deegan, R. D., Brunet, P. & Eggers, J. 2008 Rayleigh–Plateau instability causes the crown splash. arXiv:0806.3050.

Eggers, J. 1997 Nonlinear dynamics and breakup of free surface flows. *Rev. Mod. Phys.* **69**, 865–929.

Eggers, J. & Villermaux, E. 2008 Physics of liquid jets. *Rep. Prog. Phys.* **71**, 036601.

Entov, V. M. 1982 On the dynamics of films of viscous and elastoviscous liquids. *Arch. Mech. Stosow* **34** (4), 395–407.

Entov, V. M., Rozhkov, A. N., Feizkhanov, U. F. & Yarin, A. L. 1986 Dynamics of liquid films: plane films with free rims. *J. Appl. Mech. Tech. Phys.* **27** (1), 41–47.

Entov, V. M. & Yarin, A. L. 1984 The dynamics of thin liquid jets in air. *J. Fluid Mech.* **140**, 91–111.

Frankel, I. & Weihs, D. 1985 Stability of a capillary jet with linearly increasing axial velocity (with application to shaped charges). *J. Fluid. Mech.* **155**, 289–307.

Fullana, J. M. & Zaleski, S. 1999 Stability of a growing end rim in a liquid sheet of uniform thickness. *Phys. Fluids* **11** (5), 952–954.

Gorokhovski, M. & Herrmann, M. 2008 Modeling primary atomization. *Annu. Rev. Fluid Mech.* **40**, 343–366.

Hsiang, L.-P. & Faeth, G. M. 1992 Near-limit drop deformation and secondary breakup. *Int. J. Multiph. Flow* **18**, 635.

Hsiang, L.-P. & Faeth, G. M. 1995 Drop deformation and breakup due to shock wave and steady disturbances. *Intl J. Multiph. Flow* **21**, 545.

Josserand, C. & Zaleski, S. 2003 Droplet splashing on a thin liquid film. *Phys. Fluids* **15**, 1650.

Khakhar, D. V. & Ottino, J. M. 1987 Breakup of liquid threads in linear flows. *Intl J. Multiph. Flow* **13**, 71–86.

Krechetnikov, R. & Homsy, G. M. 2009 Crown-forming instability phenomena in the drop splash problem. *J. Colloid Interface Sci.* **331**, 555–559.

Lin, S. P. & Reitz, R. D. 1998 Drop and spray formation from a liquid jet. *Annu. Rev. Fluid Mech.* **30**, 85–105.

Rayleigh, Lord 1879 On the instability of jets. *Proc. Lond. Math. Soc.* **10**, 4–29.

Roisman, I. V. 2004 Dynamics of inertia dominated binary drop collisions. *Phys. Fluids* **16**, 3438–3449.

Roisman, I. V., Gambaryan-Roisman, T., Kyriopoulos, O., Stephan, P. & Tropea, C. 2007 Breakup and atomization of a stretching crown. *Phys. Rev.* E **76**, 026302.

Roisman, I. V., Horvat, K. & Tropea, C. 2006 Spray impact: rim transverse instability initiating fingering and splash, and description of a secondary spray. *Phys. Fluids* **18**, 102–104.

Roisman, I. V., Rioboo, R. & Tropea, C. 2002 Normal impact of a liquid drop on a dry surface: model for spreading and receding. *Proc. R. Soc. Lond.* A **458**, 1411–1430.

Roisman, I. V. & Tropea, C. 2002 Impact of a drop onto a wetted wall: description of crown formation and propagation. *J. Fluid Mech.* **472**, 373–397.

Roth, C. B., Deh, B., Nickel, B. G. & Dutcher, J. R. 2005 Evidence of convective constraint release during hole growth in freely standing polystyrene films at low temperatures. *Phys. Rev.* E **72**, 021802.

Rozhkov, A., Prunet-Foch, B. & Vignes-Adler, M. 2002 Impact of water drops on small targets. *Phys. Fluids* **14**, 3485–3501.

Savva, N. & Bush, J. W. M. 2009 Viscous sheet retraction. *J. Fluid Mech.* **626**, 211–240.

Taylor, G. I. 1959*a* The dynamics of thin sheets of fluid. Part 1. Water bells. *Proc. R. Soc. Lond.* A **253** (1274), 289–295.

Taylor, G. I. 1959*b* The dynamics of thin sheets of fluid. Part 2. Waves on fluid sheets. *Proc. R. Soc. Lond.* A **263**, 296–312.

Taylor, G. I. 1959*c* The dynamics of thin sheets of fluid. Part 3. Disintegration of fluid sheets. *Proc. R. Soc. Lond.* A **253** (1274), 289–295.

Thoroddsen, S. T. 2002 The ejecta sheet generated by the impact of a drop. *J. Fluid Mech.* **451**, 373–381.

Tomotika, S. 1935 On the stability of a cylindrical thread of a viscous liquid surrounded by another viscous fluid. *Proc. R. Soc. Lond.* A **150**, 322–337.

Vander Wal, R. L., Berger, G. M. & Mozes, S. D. 2005 Droplets splashing upon films of the same fluid of various depths. *Exp. Fluids* **40** (1), 33–52.

Villermaux, E. 2007 Fragmentation. *Annu. Rev. Fluid Mech.* **39**, 419–46.

Weber, C. 1931 Zum Zerfall eines Flüssigkeitsstrahles. *Z. Angew. Math. Mech.* **2**, 136–154.

Yarin, A. L. 1993 *Free Liquid Jets and Films: Hydrodynamics and Rheology*. Longman & Wiley.

Yarin, A. L. & Weiss, D. A. 1995 Impact of drops on solid surfaces: self-similar capillary waves, and splashing as a new type of kinematic discontinuity. *J. Fluid Mech.* **283**, 141–173.